New Journal of Physics

The open access journal at the forefront of physics

CrossMark

PAPER

An adjustable-length cavity and Bose–Einstein condensate apparatus for multimode cavity QED

Alicia J Kollár[1,3,4], Alexander T Papageorge[1,3,4], Kristian Baumann[1,2,3], Michael A Armen[3] and Benjamin L Lev[1,2,3]

1. Department of Applied Physics, Stanford University, Stanford CA 94305, USA
2. Department of Physics, Stanford University, Stanford CA 94305, USA
3. E. L. Ginzton Laboratory, Stanford University, Stanford CA 94305, USA
4. These authors contributed equally.

E-mail: benlev@stanford.edu

Keywords: cavity QED, BEC, phase transitions

Abstract

We present a novel cavity QED system in which a Bose–Einstein condensate (BEC) is trapped within a high-finesse optical cavity whose length may be adjusted to access both single-mode and multimode configurations. We demonstrate the coupling of an atomic ensemble to the cavity in both configurations and measure that the single-atom, $TEM_{0,0}$-mode cooperativity exceeds unity. The atoms are confined either within an intracavity far-off-resonance optical dipole trap or a crossed optical dipole trap via transversely oriented lasers. Multimode cavity QED provides fully emergent and dynamical optical lattices for intracavity BECs, in that the process of atomic self-organization may be described as a continuous symmetry breaking phase transition resulting in the emergence of a compliant lattice with phonon-like excitations. Such systems will enable explorations of quantum soft matter, including superfluid smectics, superfluid glasses, and spin glasses as well as neuromorphic associative memory.

1. Introduction

Cavity QED is a particularly attractive setting to explore many-body physics using quantum gases of neutral atoms [1]. In these systems, a laser pumps energy into cavity modes either directly via a semitransparent mirror or indirectly via coherent (Rayleigh) scattering off intracavity atoms. This light leaks out of the cavity by the same semitransparent mirrors—or via atomic spontaneous emission—and may serve as a record of the collective dynamics driven by light–matter coupling. Interaction timescales can be orders of magnitude faster than the superexchange or dipolar exchange interactions exploited in traditional optical lattice-based quantum simulators [2–4]. A non-equilibrium steady state may be reached before spontaneous emission heats the gas. Despite the driven, dissipative character of this intrinsically non-equilibrium system, statistical mechanical treatments may be employed to analyze phase transitions [5–9].

In the dispersive limit, collective dynamics are driven by the effective atom–atom coupling mediated by the exchange of photonic excitations via the resonant cavity mode(s). These atom–atom interactions are of infinite range in a single-mode Fabry–Perót cavity [10]: mean-field descriptions are adequate to describe the collective behavior since spatially inhomogeneous interaction fluctuations are not supported, aside from an underlying sinusoidal modulation. By contrast, multimode Fabry–Perót cavities—i.e., those with many degenerate modes—support shorter-ranged and strongly fluctuating interactions, as described in section 5, and may enable observations of beyond mean-field many-body physics. Quantum liquid crystals and superfluid glasses [7, 8], as well as spin glasses [11–14], may be created by scattering light into a multimode cavity via an intracavity quantum gas. Spin glasses are intimately related to architectures for neuromorphic computation, specifically Hopfield associative memories [11, 15] and 3D Ising machines [16], both of which may be created in this quantum optical setting.

Benchmarking observations of multimode cavity QED against prior, single-mode cavity experiments will prove crucial for understanding how complex beyond mean-field physics is manifest, if at all. We have therefore constructed a cavity QED apparatus that provides a unique capability: *in situ* tunability of the cavity length from the single-mode regime to multimode degeneracy, all while maintaining stability against vibration in a vacuum sufficient for quantum gas production.

We first describe the experimental apparatus, beginning with the adjustable-length and multimode cavity in section 2, including vibration support, length adjustment, locking scheme, and cavity properties. Section 3 describes the portions of the apparatus used to produce ultracold gases, transport them into the cavity, and Bose-condense them or trap them using an intracavity far-off-resonance optical dipole trap (FORT) [17]. Section 4 presents data on atomic ensemble-cavity coupling in both the single-mode and multimode configurations. Lastly, we briefly outline in section 5 how this adjustable-length and multimode cavity system might enable the creation of exotic many-body states.
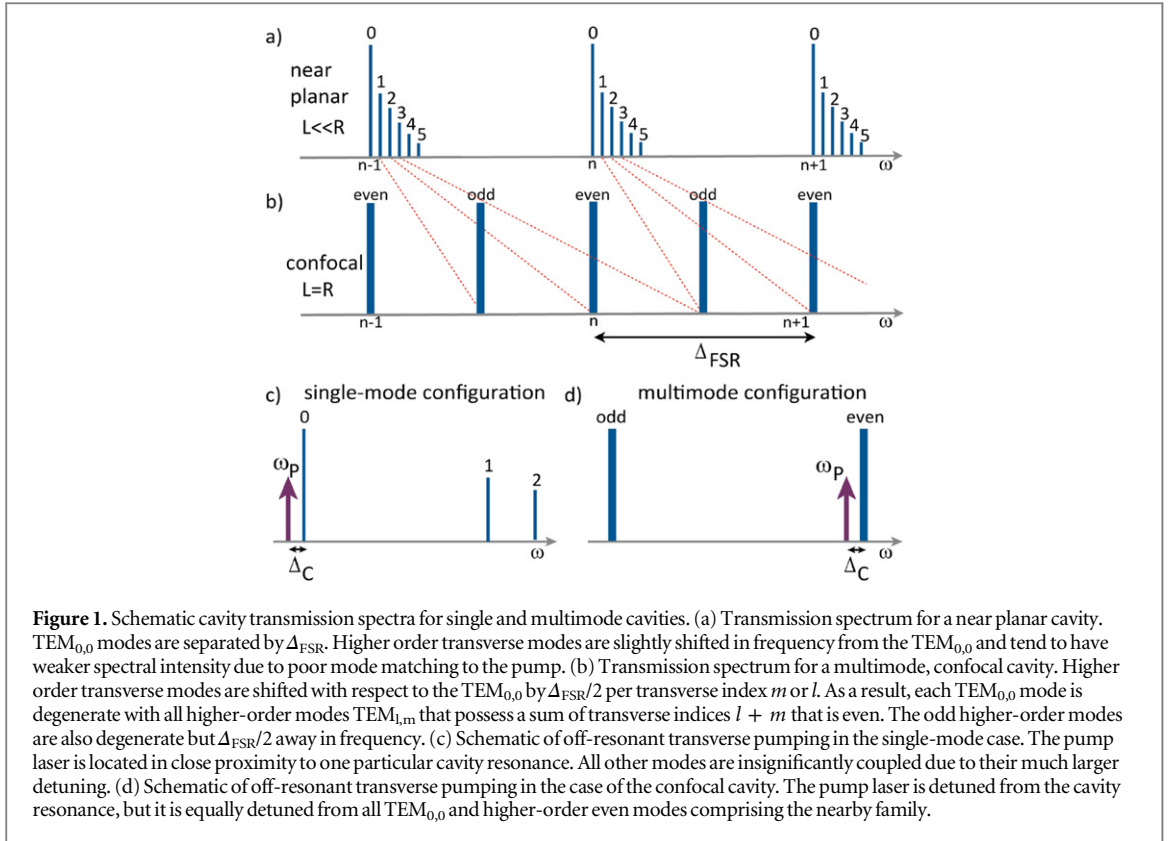
2. Adjustable-length and multimode cavity

The challenge to engineering an adjustable-length optical cavity compatible with Bose–Einstein condensates (BECs) and capable of accessing the aforementioned regimes of many-body physics is many-fold, for instance: (1) all parts—including epoxies—of the cavity assembly and vibration isolation system must be compatible with maintaining a ultrahigh vacuum (UHV), or else BEC production will not be possible. (2) Magnetic parts must be avoided to achieve precise control of the magnetic fields and gradients at the position of the intracavity atoms and to avoid inducing vibrations during rapid switching of current in nearby electromagnetic coils. (3) The long-throw actuator that moves one of the mirrors must be sufficiently stable so as not to subject the cavity to too many low-frequency mechanical resonances. Any such resonances allow ambient acoustical or seismic noise to drive the cavity below the low-pass cut-off of the filter provided by the mechanical vibration isolation stack. Canceling these transmitted vibrations via feedback to a fast, single-crystal piezo, e.g., attached to the opposing mirror, is difficult: large gain is required to compensate for the resonantly coupled noise, but that also makes it challenging to close the servo bandwidth before actuator resonances cause positive feedback oscillations. (4) To achieve a high-density of degenerate modes at the length of multimode operation, the mirror mounting procedure must provide the flexibility to angle and translate the mirrors as they become permanently affixed as the epoxy sets. (5) To maintain high-quality resonances throughout the travel of the mirror, the actuator must move with high linearity so as not to misalign the mirror. (6) The mirror spacing must be as small as possible while maintaining a large cavity finesse. This provides a large vacuum (single-photon) Rabi frequency $2g_0$, which in turn maximizes the per-atom cooperativity, $C \equiv 2g_0^2/\kappa\gamma$ [18]. This parameter sets the strength of the atom-cavity interaction versus decay rates, where γ is the atomic linewidth and the field decay rate is κ. We now describe how we meet these challenges.

2.1. Multimode versus single-mode cavities

A single-mode Fabry–Perót cavity possesses a geometrical configuration of mirrors such that families of transverse electromagnetic modes $\mathrm{TEM}_{l,m}$ differing in the sum $l + m$ resonate at intervals in frequency much larger than κ. For example, the frequency spacing between the $\mathrm{TEM}_{0,0}$ mode and the family of $l + m = 1$ of modes, i.e., $\mathrm{TEM}_{1,0}$ and $\mathrm{TEM}_{0,1}$, must satisfy $|\Delta\omega_{\{l+m=0\}-\{l+m=1\}}| \equiv |\omega_{\{l+m=0\}} - \omega_{\{l+m=1\}}| \gg \kappa$, where $\omega_{\{l+m\}}$ is the frequency of all the modes in a family whose transverse field nodes sum to $l + m$. (In the absence of astigmatism and birefringence, $\omega_{1,0} = \omega_{0,1}$.) The cavity is said to be in a single-mode configuration with respect to a pump field if the frequency detuning $\omega_P - \omega_C = \Delta_C$ of the pump laser from the single cavity mode of interest is much smaller than the frequency spacing between all other modes, e.g., if $|\Delta_C| \ll \Delta\omega_{\{l+m=0\}-\{l+m=1\}}$. See figure 1 for sketch.

Unlike single-mode cavities, multimode cavities support $\mathrm{TEM}_{l,m}$ modes resonating at the same frequency, even if they possess differing numbers $l + m$ of transverse field nodes [19]. Interactions mediated by these modes are energy degenerate, since they possess the same frequency. However, the spatial range of the effective interaction is reduced due to the exchange of photonic excitation though superpositions of these disparate mode patterns: interferences among the mutually incommensurate Hermite–Gaussian—or equivalently, Laguerre–Gaussian—mode-functions $\Xi_{l,m}$ reduce the interaction range. Specifically, the infinite-range interactions in a single-mode cavity form a complete graph of pairwise interactions weighted by the product of a single-field mode amplitude $\Xi_{l,m}(r_i)\Xi_{l',m'}(r_j)\delta_{ll'}\delta_{mm'}$. By contrast, the interactions in a multimode cavity are finite-ranged: considering the modes $\mathrm{TEM}_{m,0}$, the interactions fall with distance as $\mathrm{sinc}(\zeta\rho_{ij})/w_0$, where w_0 is the $\mathrm{TEM}_{0,0}$ mode waist, due to destructive interference among the Hermite–Gaussian cavity modes[5]. This interaction approaches

---

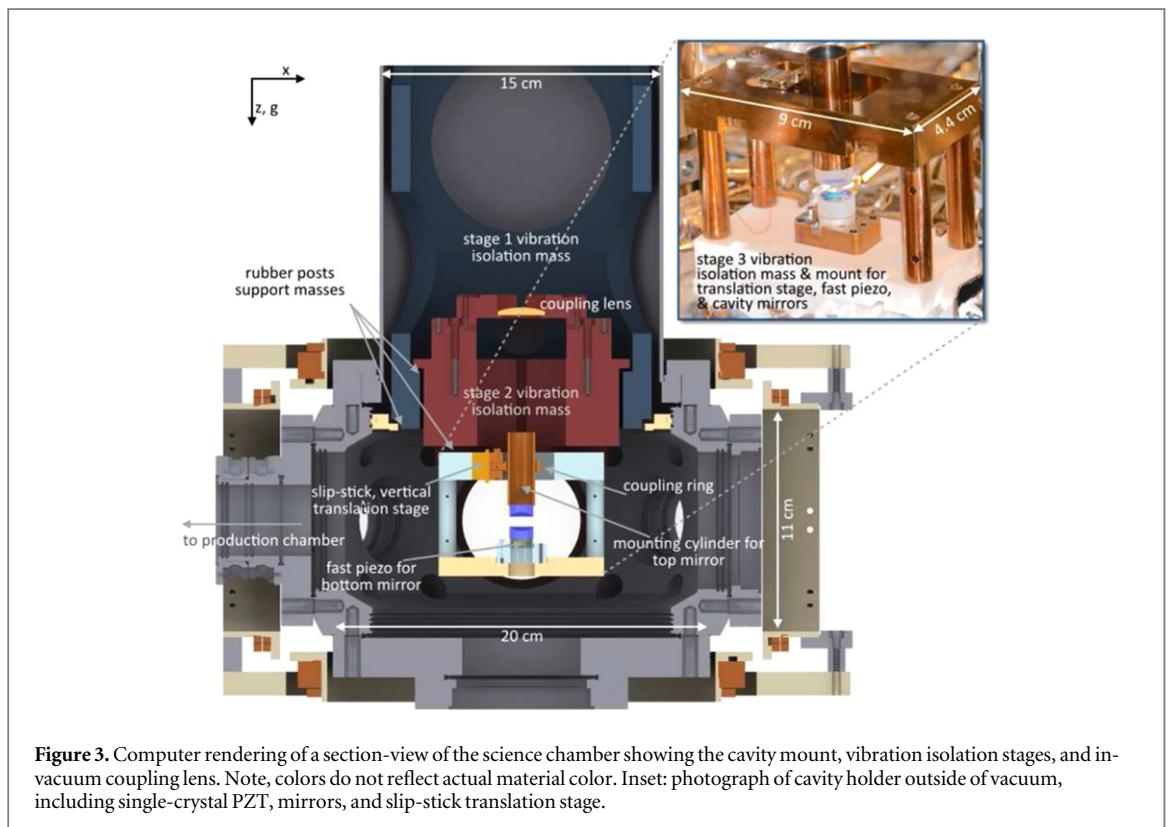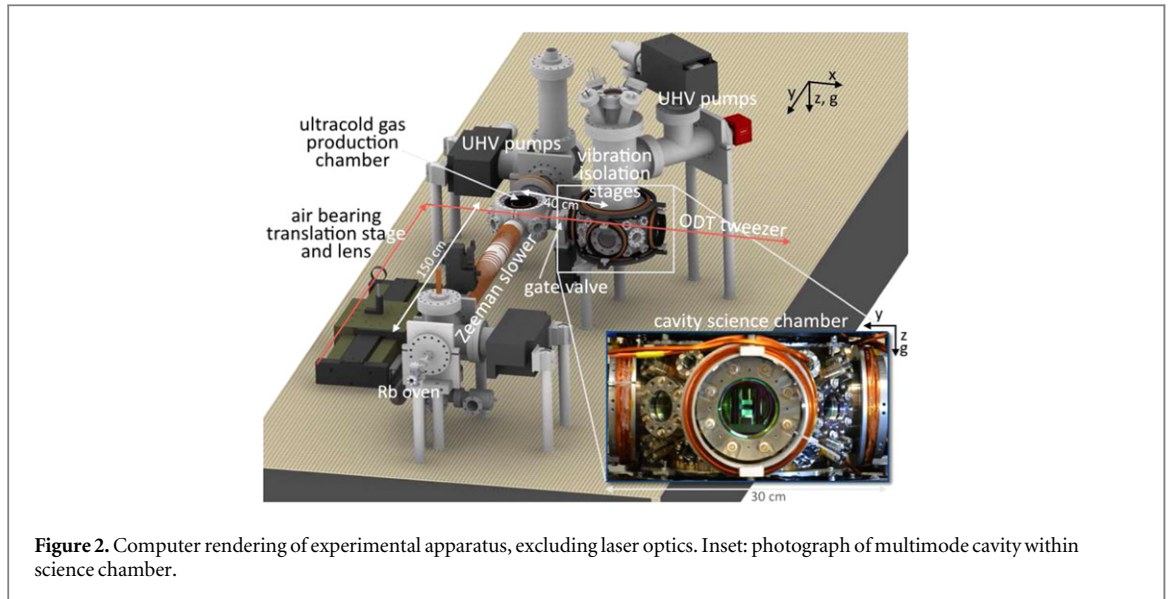[5] The interactions fall faster than a sinc-function when considering $l \neq 0$ modes.

Figure 1. Schematic cavity transmission spectra for single and multimode cavities. (a) Transmission spectrum for a near planar cavity. $TEM_{0,0}$ modes are separated by Δ_{FSR}. Higher order transverse modes are slightly shifted in frequency from the $TEM_{0,0}$ and tend to have weaker spectral intensity due to poor mode matching to the pump. (b) Transmission spectrum for a multimode, confocal cavity. Higher order transverse modes are shifted with respect to the $TEM_{0,0}$ by $\Delta_{FSR}/2$ per transverse index m or l. As a result, each $TEM_{0,0}$ mode is degenerate with all higher-order modes $TEM_{l,m}$ that possess a sum of transverse indices $l + m$ that is even. The odd higher-order modes are also degenerate but $\Delta_{FSR}/2$ away in frequency. (c) Schematic of off-resonant transverse pumping in the single-mode case. The pump laser is located in close proximity to one particular cavity resonance. All other modes are insignificantly coupled due to their much larger detuning. (d) Schematic of off-resonant transverse pumping in the case of the confocal cavity. The pump laser is detuned from the cavity resonance, but it is equally detuned from all $TEM_{0,0}$ and higher-order even modes comprising the nearby family.

a δ-function in the limit $\zeta \to \infty$. Here, ζ is proportional to the number of degenerate cavity modes, r_i is the position of the atom i, and ρ_{ij} is the separation between two atoms in the direction transverse to the cavity axis. While shorter-ranged in the transverse plane, the interaction range remains infinite and proportional to $\sin(k_0 z) = \sin(2\pi z/\lambda)$ along the cavity axis for the atomic cloud length and cavity geometry considered here. λ is the wavelength of the cavity resonance.

Multimode Fabry–Perót cavities possess special relationships between the cavity length L and the mirror radius of curvature R to ensure that the round-trip path-length of rays corresponding to distinct wavevectors **k** are equal. Common configurations are the concentric cavity $L = 2R$ and the confocal cavity $L = R$. The mirror foci of concentric cavities meet at the cavity center; the mirrors of typical concentric cavities trace out but a small solid angle of a sphere of diameter $2R$. One can see that rays with **k**'s of equal length but differing direction reflect onto themselves, and therefore modes with spot sizes smaller than the mirror diameter are simultaneously resonant. (In practice, this spot size is limited by aspheric aberration and poor mirror coating reflectivity or high absorption near the mirror edge.) The advantages of concentric cavities include small mode waists, providing larger C compared to other equal-length resonators configurations [20]. While concentric cavity modes are describable by simple Bessel functions, the condition $L = 2R$ lies at the instability boundary of two-mirror resonators [19], forcing one to set the mirror length just shy of concentriccity, $L = 2R - \epsilon$, to ensure stability, in practice.

Confocal cavities with identical mirrors, by contrast, lie between stable resonator regimes, and so their length may be continuously tuned through the multimode configuration point $L = R$. Either Hermite–Gaussian or, equivalently, Laguerre–Gaussian transverse mode functions may be used to form a complete basis of supported modes [19]. In a ray-tracing picture, each degenerate mode traces an hour-glass, bow-tie pattern [21]. The frequency interval—free-spectral range—between sets of modes of equal parity is $\Delta_{FSR} = c/2L$, with that between sets of opposite parity $\Delta_{FSR}/2$. See figure 1. This unusual property will allow us to couple the atoms to purely even parity modes or purely odd parity modes. The degenerate modes of confocal cavities, while more difficult to work with in the framework of theories employing functional integration [7, 8], provide access to the same physics as concentric cavities. We have therefore chosen to build a cavity of the confocal configuration, though our system may easily be modified—without breaking vacuum in the ultracold atom production chamber—to increase the cavity length to the concentric configuration.

2.2. Cavity science chamber

Our experimental apparatus, shown in figure 2, consists of two sections: an ultracold atom production section and a cavity science chamber. The science chamber, shown in detail in figure 3, houses the multimode cavity and the three stages of its vibration isolation stack. This section provides ample optical access for coupling light into

Figure 2. Computer rendering of experimental apparatus, excluding laser optics. Inset: photograph of multimode cavity within science chamber.

Figure 3. Computer rendering of a section-view of the science chamber showing the cavity mount, vibration isolation stages, and in-vacuum coupling lens. Note, colors do not reflect actual material color. Inset: photograph of cavity holder outside of vacuum, including single-crystal PZT, mirrors, and slip-stick translation stage.
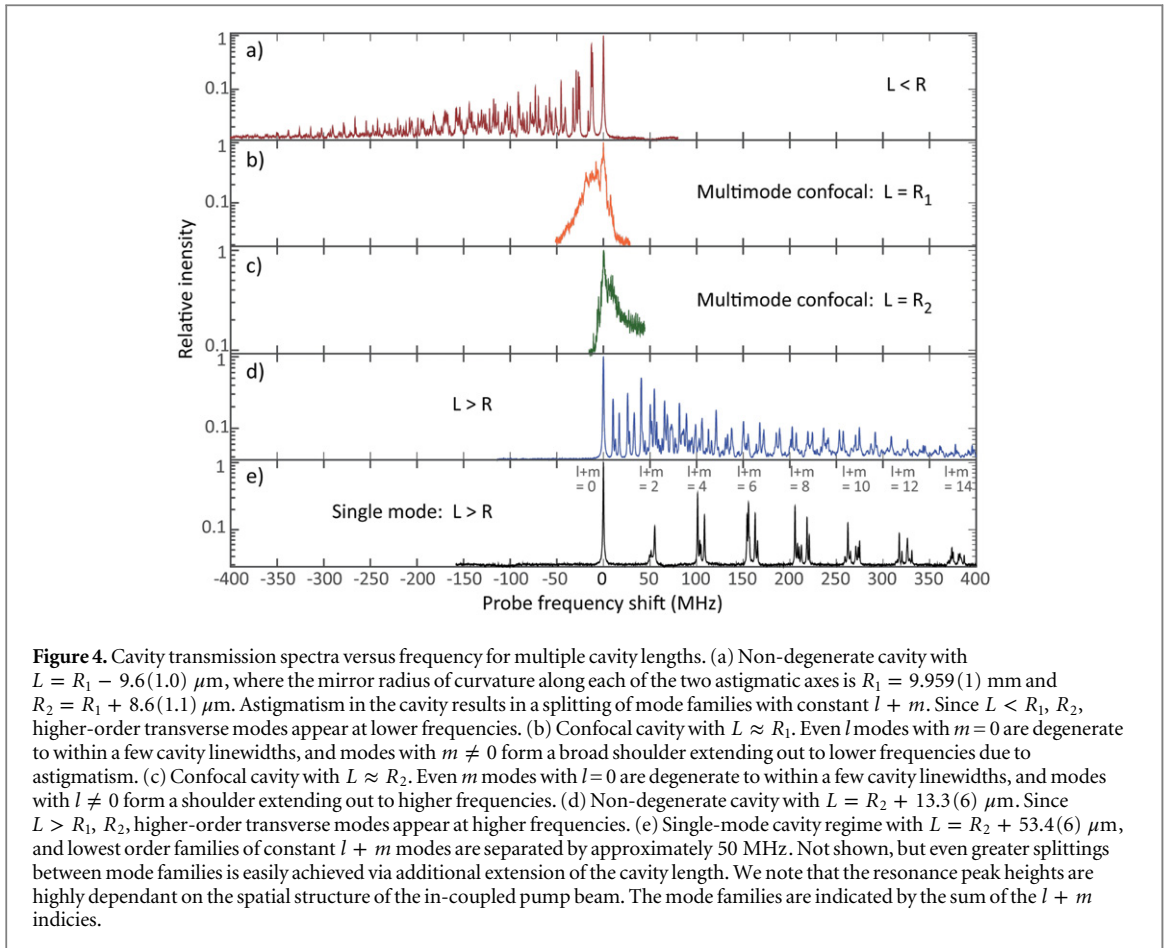
and out of the cavity, for trapping the atoms within the cavity using various configurations of optical dipole traps (ODTs), and for imaging the intracavity atomic cloud.

The vertically oriented mirrors of the high-finesse Fabry–Perót cavity are affixed to a mount constructed from non-magnetic stainless steel (SS) and Macor. This mount rests on a vibration-isolation stack within the UHV chamber for the purpose of damping environmentally coupled vibrations. Length stabilization is predominantly effected by a single-crystal PZT on which the lower mirror is affixed with UHV-safe epoxy[6]. The upper mirror is mounted to a slip-stick piezo actuator[7] with 3 mm of travel along the cavity axis. The displacements resulting from incremental actuation of the slip-stick piezo are hysteretic and non-repeatable, but the small variations may be easily compensated by applying small dc voltages to the stack piezo forming the very

---

[6] We use EPO-TEK H20E for electrical connections and EPO-TEK 301 for structural joints.

[7] Attocube ANPx51/LT/UHV.

Figure 4. Cavity transmission spectra versus frequency for multiple cavity lengths. (a) Non-degenerate cavity with $L = R_1 - 9.6\,(1.0)\ \mu$m, where the mirror radius of curvature along each of the two astigmatic axes is $R_1 = 9.959\,(1)$ mm and $R_2 = R_1 + 8.6\,(1.1)\ \mu$m. Astigmatism in the cavity results in a splitting of mode families with constant $l + m$. Since $L < R_1, R_2$, higher-order transverse modes appear at lower frequencies. (b) Confocal cavity with $L \approx R_1$. Even l modes with $m = 0$ are degenerate to within a few cavity linewidths, and modes with $m \neq 0$ form a broad shoulder extending out to lower frequencies due to astigmatism. (c) Confocal cavity with $L \approx R_2$. Even m modes with $l = 0$ are degenerate to within a few cavity linewidths, and modes with $l \neq 0$ form a shoulder extending out to higher frequencies. (d) Non-degenerate cavity with $L = R_2 + 13.3\,(6)\ \mu$m. Since $L > R_1, R_2$, higher-order transverse modes appear at higher frequencies. (e) Single-mode cavity regime with $L = R_2 + 53.4\,(6)\ \mu$m, and lowest order families of constant $l + m$ modes are separated by approximately 50 MHz. Not shown, but even greater splittings between mode families is easily achieved via additional extension of the cavity length. We note that the resonance peak heights are highly dependant on the spatial structure of the in-coupled pump beam. The mode families are indicated by the sum of the $l + m$ indicies.

same actuator. Continuously tuning the length of the cavity by hundreds of microns is straightforward and travel is sufficiently linear so as to be able to observe spectra of well-coupled modes throughout this travel range, see figure 4.

The rectangular cavity mount provides ample optical access, allowing beams to be directed at the atoms from any of the 24 viewports mounted on the spherical octagon UHV chamber. The mount hangs from the hooks of a heavy (3.5 kg) steel holder forming the second vibration isolation stage. This rests on the internal rim of a heavy (6 kg) steel cylinder forming the first vibration isolation stage. This cylinder then rests on a ledge around the inside of the UHV chamber. Small, several mm-cubed, Viton rubber pieces separate the metal pieces at each interface, thereby forming a three-stage low-pass vibration filter. The entire vibration-isolation stack can be modeled as a six-pole low-pass filter for vibrations transferred from the chamber to the cavity. Simulations indicate that all resonances lie below 200 Hz and that the cavity mount is well-protected from environmental vibrations above this cutoff. Figure 3 shows a schematic of the primary vibration isolation stack pieces. Not shown are the ion and non-evaporative getter pumps connected to the cavity science chamber, though these may be seen in figure 2. While there is a notable degree of initial outgassing from the Viton pieces and the epoxy used to construct the vibration stack and the cavity, the vacuum ion gauge nearest to the cavity reports a pressure of 1×10^{-10} Torr and the lifetime of our atomic cloud in the ODT within the cavity is 7 s. (The pressure in the production chamber is 2.5×10^{-11} Torr, several times lower than in the cavity science chamber.) This amount of time is sufficient for evaporating the already ultracold gas to quantum degeneracy, as described below, and for studying multimode cavity QED physics. Viewports above and below the cavity mirrors provide optical access to the cavity mode. Locking light, probe light, and trapping light are coupled to the cavity through these viewports. We also detect the transmission of cavity fields through these viewports with either CCD cameras, single photon counters, or photodiodes. The upper viewport is 49 cm from the cavity mirror: to prevent the rapid divergence of the beam we installed an in-vacuum coupling lens to approximately collimate the vertical cavity output. The lower viewport is sufficiently close to the bottom mirror to render an in-vacuum lens unnecessary.

Alignment of the mirrors for optimal multimode operation is performed before insertion of the cavity mount into the UHV chamber. The inset in figure 3 shows the cavity outside the UHV chamber. We first epoxy the lower mirror to the 5 mm-long cylindrical single-crystal fast piezo, which itself has been epoxied to the SS mount connecting to the Macor base of the cavity mount. We next align the upper mirror to this fixed lower

mirror. To optimize the angle and transverse position of the upper mirror, the edge of its flat side is first epoxied to the end of a 3.9 cm-long SS cylinder possessing an inner diameter sufficiently large so as not to obscure cavity transmission. This SS cylinder is then slipped through a 1.5 mm-larger-diameter mounting ring. This ring is screwed onto the face of the vertically mounted slip-stick piezo actuator. The opposite end of the SS cylinder is temporarily held by a positioning stage, and the gap between it and the mounting ring allows us to adjust both the three-axis position and angle of the mirror while the epoxy filling the gap between the cylinder and ring sets. For maintaining proper alignment, we monitor cavity transmission resonances at 780 nm while the epoxy sets, adjusting the positioning stage as needed. We ensure optimal alignment of the mirror with respect to the lower mirror with this procedure, maximizing mode density at the critical length for multimode operation while ensuring good coupling as the slip-stick actuator tunes the cavity toward and away from the $L = R$ condition.

In-vacuum length stabilization of the cavity is achieved by deriving an error signal using the Pound–Drever–Hall method [22, 23] with 1560 nm light resonant with the $\text{TEM}_{0,0}$ mode of the cavity. Fast feedback is applied to the small single-crystal piezo on the lower mirror. Slow, but large-dynamic-range feedback is applied to the piezo stack in the slip-stick translation stage that actuates the upper mirror. Measurements of the vibration characteristics of the cavity were obtained by loosely locking an optical interferometer to the flat backfaces of each mirror. The amplitude and phase excursions of the interference fringes, when driven by a swept sine-wave, provided an estimate of the transfer functions of the two actuators. Two prominent features were found: a 120 Hz mechanical resonance originating from the slip-stick translation stage and a 3.5 kHz dispersive resonance arising from the coupling of the single-crystal PZT and its mount. An electronic feedback controller was designed based on these observations, incorporating an integrator at dc and open-loop dc gain only limited by the constituent electronic components. Two additional poles in the transfer function between 10 and 100 Hz serve to lower the gain profile rapidly over the next two decades. Two zeros in the transfer function near 1 kHz recover phase margin and result in a stable unity gain point near 10 kHz. The electronic controller also incorporates active resonant filters to provide additional gain to combat the noise induced by the resonance at 120 Hz and to provide the appropriate phase and gain to cancel the 3.5 kHz dispersive resonance. The combination of these elements allows us to achieve length stabilization with rms deviation of the cavity length of 1.8(2) pm (71(5) kHz at 780 nm) as measured in via the in-loop error signal. This results in a cavity stability nearly 4× smaller than the intrinsic cavity linewidth 2κ at 780 nm, whose measurement we provide in the next section.

Light at the wings of the 1064 nm 9.8 W ODT transport beam 'tweezer' heats the cavity when this beam is focused 40 cm away in the ultracold atom production chamber. The heating ceases after the focus is translated closer to the cavity, but in the meantime, thermal expansion causes the cavity length to decrease. The length can decrease further than the dynamic range of the fast piezo, at which point cavity lock is lost. To counter this drift, we complement the fast piezo feedback with an extremely slow feedback—unity gain point of 1 Hz—to the piezo stack internal to the slip-stick positioning stage. This prevents the dc component of the fast piezo feedback voltage from railing. These two feedback loops provide robust locking of the cavity length throughout the 16 s BEC experimental cycle over the course of an afternoon.

Our cavity enjoys a single-atom cooperativity greater than unity, as we will show below. To the best of our knowledge, only two other *in situ* adjustable-length high-finesse cavities have been built for cavity QED research, though for single-mode operation [24, 25]. Strongly coupled cavity QED with a family of near-degenerate higher-order modes and a single atom was explored in reference [26]. Near-confocal cavities with thermal atoms were explored in references [27–29, 38, 39].

2.3. Cavity finesse, mode structure, astigmatism, and birefringence

The cavity finesse was measured by means of ring-down spectroscopy of the cavity transmission [30]. The decay times obtained from these measurements, in conjunction with the cavity lengths obtained from measurements of Δ_{FSR}, reveal a finesse of the $\text{TEM}_{0,0}$ mode at 780 nm to be $5.72(2) \times 10^4$. Similar measurements reveal the finesse at 1560 nm to be $1.22(1) \times 10^4$ for the same $\text{TEM}_{0,0}$ resonance. The resulting κ's are $2\pi \times 132(1)$ kHz and $2\pi \times 617(3)$ kHz, respectively. The mirrors exhibit a total round trip loss of 54.9(2) ppm at 780 nm.

We probe the cavity by locking it to a weak 1560 nm laser coupled to a $\text{TEM}_{0,0}$ resonance while addressing the cavity with 780 nm light produced by doubling this same laser. Using the slip-stick translation stage, we measured transmission spectra in the three regimes of intermode spacing of interest to our future cavity QED experiments: confocal degeneracy of one family of modes, mode separation larger than 2κ and on the order of an atomic linewidth, and modes far apart from one another and satisfying the single-mode criterion $|\Delta_C| \ll \Delta\omega_{\{l+m=0\}-\{l+m=1\}}$ with $\Delta_C \leqslant 10$ MHz. The results of these measurements are shown in figure 4, and the higher-order mode peak heights vary due to imperfect mode-matching of the input mode, which nominally has a Gaussian waist slightly bigger than the spot size of the $\text{TEM}_{0,0}$ mode at the mirror face. The use of the locking laser as the source for the probe laser ensures that the cavity remains stable with respect to the probe light

despite the potential drift of the locking laser. The frequency drift of this narrow, temperature-stabilized fiber laser is slow and fractionally insignificant in the large atomic detuning limit.

Under the paraxial approximation, the transverse mode frequencies of a Fabry–Pérot cavity made from parabolic mirrors are

$$f_{nlm} = \frac{c}{2L}\left(n + \frac{m + 1/2}{\pi}\theta_m + \frac{l + 1/2}{\pi}\theta_l\right), \tag{1}$$

where $\theta_i = \arccos\sqrt{\left(1 - \frac{L}{R_{i1}}\right)\left(1 - \frac{L}{R_{i2}}\right)}$ and R_{ij} is the radius of curvature of the jth mirror in the i direction [19]. The ideal confocal cavity corresponds to the condition $\theta_l = \theta_m = \pi/2$ such that the resonance frequency is unchanged as long as $n + (m + l)/2 = \text{constant}$.

In practice, however, highly polished mirror substrates are spherical rather than parabolic, and this spherical aberration reduces the number of supportable higher-order modes [20]. Moreover, mirror substrates may not be cylindrically symmetric due to mounting stress or the opposing mirrors may be mounted off-axis and at a relative angle. Consequently, they exhibit astigmatism, meaning that the cavity has different radii of curvature along different transverse axes. In this case $\theta_l \neq \theta_m$, with, say, θ_m corresponding to the direction with maximum R and θ_l corresponding to the direction with minimum R, or vice versa. In such cases, it is no longer possible to ensure that f_{nlm} only depends on $n + (m + l)/2$: the two transverse degrees of freedom are no longer equivalent. The astigmatic cavity then exhibits two confocal degeneracy points: one with degenerate l modes and $\theta_l = \pi/2$, and one with degenerate m modes and $\theta_m = \pi/2$. Equation (1) may now be rewritten in terms of a frequency shift proportional to $m + l$ combined with a correction along one of the transverse axes:

$$f_{nlm} = \frac{c}{2L}\left(n + \frac{m + l}{\pi}\theta_l + \frac{l}{\pi}\xi + \frac{2\theta_l + \xi}{\pi}\right), \tag{2}$$

where $\theta_m = \theta_l + \xi$.

Our cavity is found to display a small amount of astigmatism—perhaps due to mounting stress or imperfections in the manufacturing—with major and minor axes located at ∼45° to the science chamber principle axes; see figure 3. The two radii of curvature, measured by the length of the cavity at the two degeneracy conditions, are $R_1 = 9.959(1)$ mm and $R_2 = R_1 + 8.6(1.1)\ \mu$m. The respective spectra for these lengths are shown in figures 4(b) and (c). They are characterized by a single peak of nearly degenerate modes next to a broad shoulder of modes extending out to either lower or higher frequencies. The modes around the sharp peak are associated with the family of modes satisfying the degeneracy condition of one of the astigmatic axes, while the broad pedestal of nearly degenerate modes to the side is associated with the unmet degeneracy condition of the other astigmatic axis. Changing the cavity length from that shown in figures 4(b)–(c) reverses the family of modes—l versus m—that satisfies the degeneracy condition. The mode spectra of each family exhibit small deviations from the description of an ideal, fully linear, astigmatic cavity. This is likely due to spherical aberrations and mirror imperfections [21].

The cavity is effectively single mode at a large distance from confocallity, and the difference between the major and minor radii of curvature becomes negligible compared to $L - R$. The astigmatism then appears as a dispersion of spectrally isolated families of modes with constant $l + m$, as in figure 4(e). We note that much larger splittings between families of modes are possible via further translation of the positioning stage.

The maximum number of degenerate modes in the cavity is limited by the mirror imperfections which cause the finesse to decrease with increasing transverse mode index and by spherical aberrations which introduce non-linearities in f_{nlm}. We will assess in future work where the limit in the number of supportable modes lies for this cavity. However, we can obtain a rough estimate by noting the largest index mode we image on a CCD camera at a length just shy of confocallity. Unlike for a concentric cavity, the waists of the modes of a confocal cavity do not diverge at the mirror upon reaching the $L = R$ degeneracy point, and so we can assume that any mode supported at $L = R \pm \epsilon$ will likely remain so at $L = R$. We find that l and m of up to order 50 each may be observed, providing a rough estimate of $lm/4 \approx 10^3$ as the number of same-parity modes supported within a ∼50 MHz bandwidth in figures 4(b) and (c).

The cavity exhibits no measurable birefringence; it is therefore capable of supporting both linearly and circularly polarized modes since there is no frequency splitting between modes of orthogonal polarization.

2.4. Cavity dispersion

The high reflectivity of the cavity mirrors is obtained via a multilayer dielectric stack which acts as an interference filter. The characteristics of this filter, unlike a simple metal mirror, are strongly wavelength dependent [30]. The penetration depth of light into the dielectric stack is different at 780 versus 1560 nm. As a result, the effective length of the cavity is different at these two wavelengths. To first order in small changes δL of the cavity length, and ignoring the Gouy phase, the line shift of the cavity obeys the following relation: $\delta \nu/\nu = \delta L/L$ with

$\delta\nu_{780} = 2 \times \delta\nu_{2 \times 780 = 1560}$. This is true in the absence of any dispersion in the effective cavity length. However, real cavity coatings exhibit dispersion and $L_{1560} = L_{780} + \Delta L$, where ΔL is a required correction to obtain the frequency relationship between cavity resonances at the two wavelengths: $\delta\nu_{780} = (2 + \epsilon_D)\delta\nu_{1560}$. In addition to modifying the behavior of the cavity with respect to length changes, the dispersion of the cavity length also results in an absolute frequency offset Δ_D between the frequencies at which the 1560 nm laser and the doubled light are resonant with the cavity. In order to have resonant probe light at 780 nm and locking light at 1560 nm, sidebands must be introduced onto the 1560 nm laser at either Δ_D or $\Delta_D - \Delta_{FSR}/2$.

We find the factor ϵ_D by varying the frequency of the locking sideband required to address the cavity resonance at 1560 nm and then measuring the resultant translation of the 780 nm cavity resonance when the cavity is locked at this new frequency: $\epsilon_D = 5.83(5) \times 10^{-4}$. This information, together with the laser frequency and Δ_D, provides sufficient information to infer that the effective length difference $\Delta L = 2.78(3)\ \mu$m. This length difference is beneficial for locking because the cavity is not simultaneously degenerate for both wavelengths. Instead, the 1560 nm resonances are separated by $\sim 4.5\kappa$ when the cavity is degenerate at 780 nm, at the $L = R_2$ condition.

3. Ultracold gas production, transport, condensation and intracavity trapping

The creation of ultracold gases in the production chamber follows the work of Lin *et al* [31]. An atomic beam, decelerated by a Zeeman slower [32], loads ^{87}Rb into a magneto-optical trap (MOT) at the center of the production chamber's trapping region. See figure 2. Subsequently, the atoms are optically pumped to the $|1, -1\rangle$ state. Quickly thereafter, we increase the MOT's magnetic quadrupole field to obtain a gradient of 195 G cm^{-1}. This traps approximately one billion atoms in the $|1, -1\rangle$ state. Linearly ramping the RF frequency in coils external to the chamber from 25.5 to 5.5 MHz over 5.7 s produces an evaporatively cooled cloud of 8×10^7 atoms at 40 μK. An off-resonant ODT is tightly focused below the center of the quadrupole trap, and the atoms are directly loaded into this ODT during the course of the evaporation. We use this ODT as an optical tweezer for transporting the atoms into the cavity science chamber. It employs 9.8 W of 1064 nm laser light focused to waists of 50 and 73 μm in the horizontal and vertical directions, respectively. Loading into the ODT from the magnetic trap is performed by significantly reducing the quadrupole gradient over 1 s to a value just supporting the atoms against gravity. In this configuration, the quadrupole trap provides confinement in the weakly trapped, axial direction of the ODT beam. By lowering the optical power, the atoms can undergo efficient optical evaporation to high phase-space density. We have obtained a BEC of 1×10^6 atoms at 200 nK in the production chamber by further reducing the ODT power.

However, creating BECs before ODT transport to the cavity science chamber is counter-productive, as three-body collisions heat the gas during transport [33]. Rather, we evaporate to 8 μK above $T_c = 1.6\ \mu$K and transport 6×10^6 atoms to the cavity science chamber by translating the last focusing lens of the ODT. This lens is mounted on an air bearing translation stage. The stage provides a translation of the lens and of the ODT focus over a distance of 35 cm in 4.3 s. The position of this beam is adjusted to maximize loading of atoms into the ODT while maintaining a transport trajectory whose final location is the center of the multimode cavity. The motion of the stage is chosen to be a smooth function defined by three sections of constant acceleration, with the central section having zero acceleration. The parameters of this curve were chosen so as to maximize transfer of atoms into the science chamber. The overall transfer efficiency 30% is currently limited by magnetic field gradients, background gas collisions, and mechanical excitation.
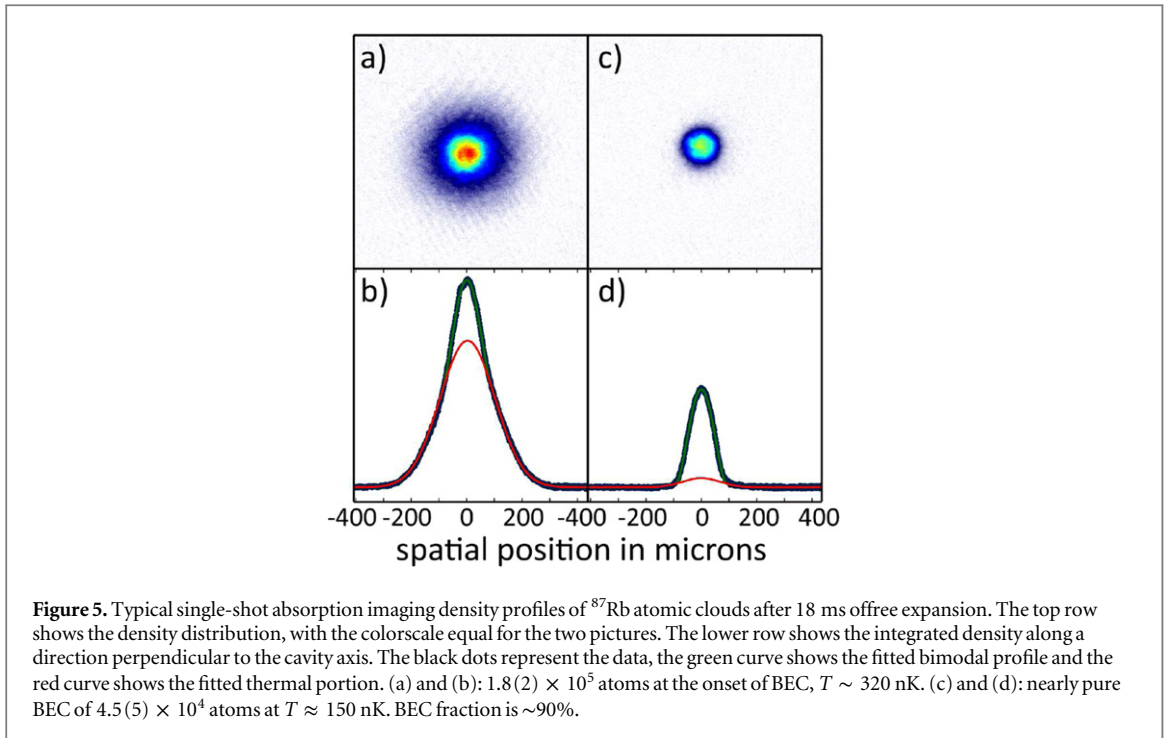
The two sections of the apparatus, the ultracold atom production chamber and the cavity science chamber, are separated by a gate valve, allowing us to break vacuum in one without disturbing the other. This feature will prove useful for modifying the cavity, if for instance we want satisfy the concentric criterion $L = 2R$ or exchange the mirrors with ones of differing finesse or R.

3.1. BEC production within the cavity
Once the atomic cloud is positioned between the mirrors in the science chamber, a second 1064 nm laser beam crosses it to confine the atoms. This beam is circular with a Gaussian waist (1/e radius) of 48 μm. Forced evaporation in this crossed ODT produces a nearly pure BEC of $4.5(4) \times 10^4$ atoms at density $4.7(5) \times 10^{14}$ cm^{-3}, as shown in figure 5. The trap frequencies are 145(5), 115(1), and 167(2) Hz in $\hat{x}$, $\hat{y}$, and $\hat{z}$, respectively. We expect to achieve pure condensates with 10^5 atoms after performing additional evaporation optimization. The total time to achieve a BEC within the cavity, starting from MOT loading, is 16 s.

3.2. Intracavity FORT
For ease of coupling to the cavity mode at 780 nm, we can also load a thermal gas into an intracavity FORT formed with the 1560 nm locking light in the TEM$_{0,0}$ mode. To do so, we increase the power of the locking laser

Figure 5. Typical single-shot absorption imaging density profiles of ^{87}Rb atomic clouds after 18 ms offree expansion. The top row shows the density distribution, with the colorscale equal for the two pictures. The lower row shows the integrated density along a direction perpendicular to the cavity axis. The black dots represent the data, the green curve shows the fitted bimodal profile and the red curve shows the fitted thermal portion. (a) and (b): $1.8(2) \times 10^5$ atoms at the onset of BEC, $T \sim 320$ nK. (c) and (d): nearly pure BEC of $4.5(5) \times 10^4$ atoms at $T \approx 150$ nK. BEC fraction is ~90%.

until the steady state circulating power provides a trap depth of $5.2(1.3)\,\mu$K. The transport ODT brings atoms into the science chamber and holds the cloud within the cavity mode. Addition of a second ODT beam crossing the first increases the mode matching between the 1064 nm trap and the 1560 nm cavity mode. Optical evaporation with the crossed 1064 nm beams loads atoms in the intracavity FORT, resulting in $2.5(2) \times 10^5$ atoms at $1.8(5)\,\mu$K confined in the 1560 nm standing-wave TEM$_{0,0}$ cavity mode. The temperature and atom number uncertainties, as well as the relatively high final temperature, are dominated by the lack of intensity stabilization and dynamical intensity adjustment of the FORT power, all of which will be added in the near future.
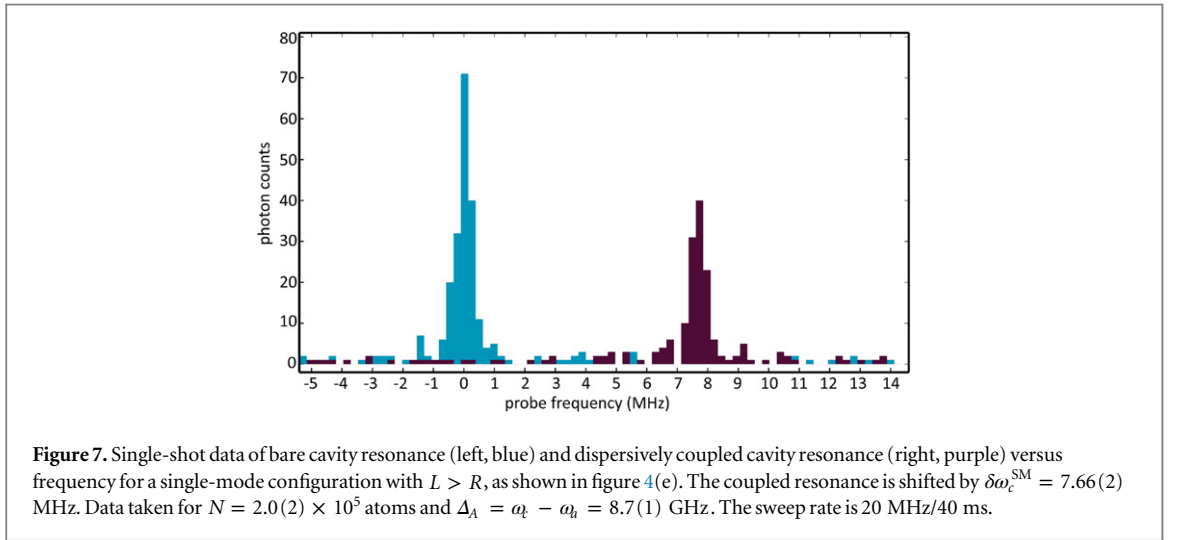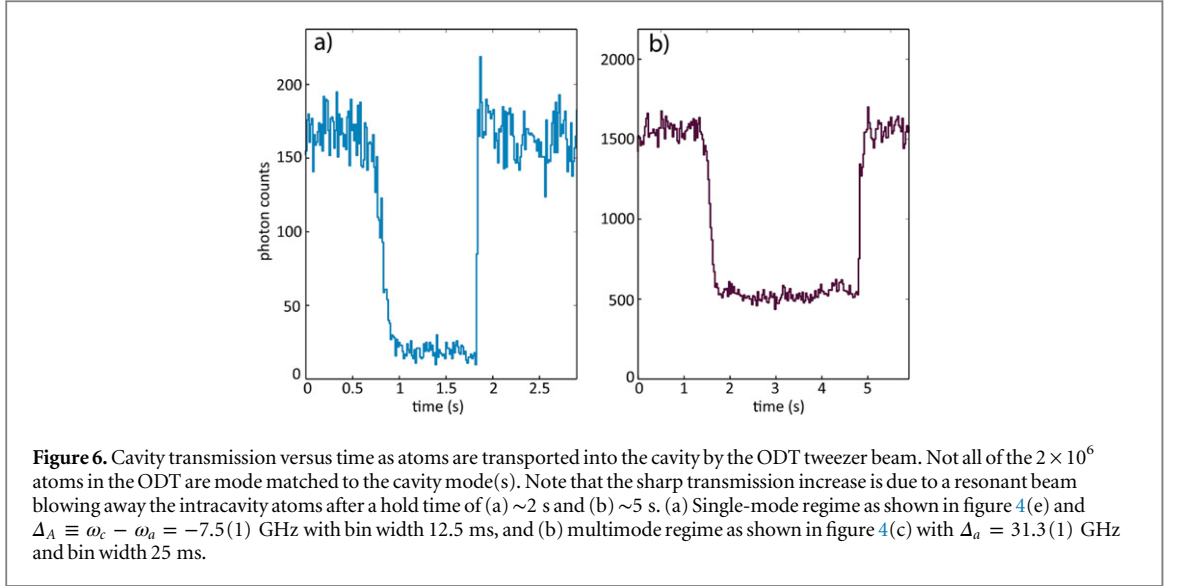
The atoms in the FORT are thermal and the in-trap density distribution obeys Boltzmann statistics with $\rho(\mathbf{x}) = \exp(-V(\mathbf{x})/T)$, where $V(\mathbf{x})$ is the standing-wave optical potential of the FORT. The resulting atomic density distribution is Gaussian, assuming a harmonic approximation to the potential. Such an approximation is valid as long as the atoms are sufficiently cold so as to localize close to the potential minima. We choose to operate at larger trap depth, though lower atom number, in the experiments discussed below. Since the atoms are loaded into the FORT from an ODT with waists larger than $\lambda/2$, the atoms will occupy multiple wells of the FORT. The waist of the 1560 nm TEM$_{0,0}$ cavity mode is $\sqrt{2}$ larger than the 780 nm TEM$_{0,0}$ mode waist: the FORT waist is $35\sqrt{2} = 50\,\mu$m. For the trap parameters used below—$V_{\text{FORT}} = 22(6)\,\mu$K and $T = 5(1)\,\mu$K—the atomic density distribution has a transverse waist of $\sim 17\,\mu$m, which is smaller than the 35 μm waist of the 780 nm mode.

4. Atomic ensemble-cavity coupling in single-mode and multimode configurations

We now present results demonstrating the coupling of an atomic ensemble trapped in the intracavity FORT to the cavity, both in the multimode and in the single-mode configurations.

4.1. Atomic ensemble transiting cavity mode(s)
The first measurement is of the transmission of the cavity as atoms are transported into the cavity by the ODT tweezer. As shown in figure 6 for both the single mode and the mulitmode configurations, at $t = 0$, light is injected into the cavity on resonance and the transmission is recorded on a single photon counter. As the atoms enter the cavity, the atomic ensemble-cavity interaction dispersively shifts the cavity line out of resonance with the probe laser and the transmission drops smoothly [34–36]. After a hold time, the atoms are rapidly removed from the cavity by a resonant laser oriented transverse to the cavity axis. After this the transmission sharply returns to the original value. For the single-mode configuration, 10% of photons leaking from the cavity mode are detected by the single-photon detector. This detection efficiency includes loss due to transmission, mode-matching, and the imperfect quantum efficiency of the detector. In the multimode configuration, the detection

Figure 6. Cavity transmission versus time as atoms are transported into the cavity by the ODT tweezer beam. Not all of the 2×10^6 atoms in the ODT are mode matched to the cavity mode(s). Note that the sharp transmission increase is due to a resonant beam blowing away the intracavity atoms after a hold time of (a) ∼2 s and (b) ∼5 s. (a) Single-mode regime as shown in figure 4(e) and $\Delta_A \equiv \omega_c - \omega_a = -7.5(1)$ GHz with bin width 12.5 ms, and (b) multimode regime as shown in figure 4(c) with $\Delta_a = 31.3(1)$ GHz and bin width 25 ms.

Figure 7. Single-shot data of bare cavity resonance (left, blue) and dispersively coupled cavity resonance (right, purple) versus frequency for a single-mode configuration with $L > R$, as shown in figure 4(e). The coupled resonance is shifted by $\delta\omega_c^{SM} = 7.66(2)$ MHz. Data taken for $N = 2.0(2) \times 10^5$ atoms and $\Delta_A = \omega_t - \omega_a = 8.7(1)$ GHz. The sweep rate is 20 MHz/40 ms.

efficiency is ∼10% for the lowest order modes, but decreases for higher order modes due to poor mode-matching into the detector.

4.2. Single-mode cavity dispersive shift

In a second series of experiments, we measure the dispersive shift of the cavity resonance with atoms confined within the intracavity FORT and with a pump field injecting 1.7(3) photons when on resonance with the cavity. In the single-mode cavity case of figure 7, we observe that coupling of the atomic ensemble to the cavity shifts the cavity resonance by $\delta\omega_c = 7.66(2)$ MHz $\gg \kappa$, as expected from considering the normal-mode spectrum of the Tavis–Cummings model of single-mode, multi-atom cavity QED [34, 36]. Using numerical simulations of the optical Bloch equations [36], we determine that the observed polariton shift is only ∼1% smaller than it would be in the weak-driving limit. This limit is defined as that of a pump field injecting much less than one intracavity photon when the pump is on resonance with the cavity. Nonlinear saturation effects are absent in this limit.

We use the single-mode cavity dispersive shift to obtain a measurement of the single atom coupling constant g_0 via $\delta\omega_c^{SM} = N_{\text{eff}} g_0^2 / \Delta_A$, where $N_{\text{eff}} = \alpha_{0,0} N$ is the effective number of atoms coupled to the cavity TEM$_{0,0}$ mode and $\Delta_A = \omega_t - \omega_a$. The overlap $\alpha_{0,0}$ of the atomic cloud confined within the intracavity 1560 nm standing-wave FORT with the electric field of the 780 nm cavity standing-wave is given by [37]:

$$\alpha_{0,0} = \frac{1}{2} \frac{1 + e^{-4/\eta}}{1 + 2/\eta} = 0.5(1), \tag{3}$$

with $\eta = V_{\text{FORT}}/k_B T$. The trap depth V_{FORT} of our FORT is 22(6) μK and the atoms are at $T = 5(1)\,\mu$K. The value of g_0 is inferred from the measurements $N = 2.0(2) \times 10^5$ and $\Delta_A = 8.7(1)$ GHz and the use of the

appropriate transition matrix elements for the D2-line of ^{87}Rb at this detuning, the polarization of the pump beam, and the direction of the quantization axis set by an applied magnetic field. We determine $g_0 = 2\pi \times 1.0(1)$ MHz on the $|5S_{1/2}, F = 2, m_F = -2\rangle \rightarrow |5P_{3/2}, F = 3, m_F = -3\rangle$ cycling transition or $g_0 = 2\pi \times 7.2(8) \times 10^5$ Hz on the $|5S_{1/2}, F = 1, m_F = -1\rangle \rightarrow |5P_{3/2}, F = 2, m_F = -2\rangle$ transition. The expected theoretical value of the coupling is $g_0' = \sqrt{\mu^2 \omega_t / \hbar \epsilon_0 V}$, where μ is the transition matrix element, $V = \pi w_0^2 L/4$ is the mode volume and $w_0 = \sqrt{R\lambda/2\pi} = 35\,\mu$m is the mode waist (1/e mode radius). Based on the measurements of the cavity R and L mentioned above, $g_0' = 2\pi \times 1.47$ and $g_0' = 2\pi \times 1.04$ MHz respectively for the two transitions. We note that the single-atom cooperativity when driving on the $|5S_{1/2}, F = 2, m_F = -2\rangle \rightarrow |5P_{3/2}, F = 3, m_F = -3\rangle$ transition is $C \approx 2.5$.

The disparity between the inferred g_0's and the corresponding theoretical g_0''s is likely due to an overestimate of $\alpha_{0,0}$. The harmonic approximation to $V(x)$ is not quite accurate for these small ratios of trap depth-to-temperature. A breakdown of this approximation would tend to lower $\alpha_{0,0}$, which in turn would increase the inferred g_0's to be closer to the expected g_0''s. A more accurate calculation of $\alpha_{0,0}$, together with improved stability of the FORT power and better measurements of the intratrap T and N of the atoms, will allow us to obtain a more accurate value of g_0.

5. Prospects for beyond mean-field physics with multimode cavity QED

We now describe some of the exotic many-body states that may be accessible with BEC-multimode cavity QED systems, as proposed in references [7, 8, 11–15]. These systems consist of a cavity pumped indirectly by coherently scattering light off intracavity atoms [5, 20, 27, 28, 40]. As mentioned in section 1, beyond mean-field physics may play a role in the system organization due to the fact that multiple degenerate modes of the cavity support localized fluctuations. To qualitatively explain this in more detail, we first describe self-organization of atoms within a single-mode cavity before following the analyses given in [7, 8].

The infinite-range atom–atom interaction mediated by the off-resonant scattering of pump photons induces an instability in the otherwise homogeneous density of the gas above a critical threshold intensity of this pump field [5, 28, 40]. The atoms tend to self-organize with λ-periodicity in one of the two checkerboard patterns formed by the interference of the pump and cavity fields. While the amplitude of both the cavity field and the modulated atomic density emerge due to the light–matter interaction, the spatial structure is predetermined by the cavity geometry. The atoms have only one of two ways to organize and no small deformation of the atomic arrangement connects the two patterns. The process of self-organization is therefore one of discrete symmetry-breaking. While this dynamical instability to self-organize may be considered a (second-order) phase transition, the organized phase does not possess the rigidity or compliance of a true crystalline solid: there are no phonon-like excitations of small deformations. This second-order mean-field transition in a single-mode cavity is heralded by superradiance and may be described in the framework of the Tavis–Cummings model or the Hepp–Lieb–Dicke model [5, 28, 40–53]. Atomic BECs have been placed inside Fabry–Perót cavities [54, 55], and superradiance arising from atomic density instabilities has also been observed in transversely pumped ring cavities [56, 57]. Self-structuring involving continuous symmetry breaking has been observed in cavity-less pumping of thermal gases in free space [58, 59] and near a mirror [60, 61].

The situation of a transversely-pumped multimode cavity is quite different. The atomic density may self-organize into the checkerboard pattern of any mixture or coherent superposition of the large number of degenerate modes. So in addition to the discrete $\mathbb{Z}_2$ symmetry of the λ-period lattice, a quasi-continuous symmetry is broken. This symmetry may best be viewed in a quasimomentum picture [7, 8]: The density of the atoms ρ may be decomposed into the basis of the TEM$_{l,m}$ mode functions; the mode indices l, m, n now serve as the axes of a quasimomentum space, where n is the number of longitudinal nodes along the cavity axis. For a gas confined in a 2D-plane normal to the pump field wavevector, we may write $\rho = \sum c_{m,n}\rho_{n,m}$, where we have taken the direction associated with l to point perpendicularly to this plane. It may be shown that the 'soft' modes the atoms prefer to self-organize within satisfy an equation of quasimomentum conservation $n + (l + m)/2 = k_0 R$ for a confocal cavity $L = R$ [7, 8]. ($n + l + m = k_0 R$ for a concentric cavity $L = 2R$.) This equation is none other than the characteristic equation for the axial-plus-transverse modes of a Fabry–Perót cavity, equation 1 [19].

For $l = 0$, the soft modes span two lines in the $n - m$ quasimomentum plane, intersecting at $n = k_0 R$. The $\mathbb{Z}_2$ symmetry is represented in the reflection of these lines about the m-axis, i.e., in the $-n$ portion of the plane. (The validity of allowing this index to be negative is more clear when using a Laguerre–Gaussian mode basis.) Dominant interactions exchange quasimomentum among these sets of points. Energetically costly interaction fluctuations exchange quasimomenta located above this 2D-plane via modes with non-zero l. These fluctuations are sufficiently strong so as to renormalize the Landau coefficients in the system's free energy, converting what was a second-order phase transition into a weakly first-order transition, as determined from a functional

integration analysis and following the renormalization group program laid out by Brazovskii for an analogous, classical soft matter system [62, 63].

This intriguing quantum Brazovskii transition, a rare example of a fluctuation-induced first-order transition, is very much a non-mean-field transition. Not only is the threshold of the transition renormalized upward, but the actual character of the transition—first versus second-order—differs from the single-mode case. Moreover, this weakly first-order phase transition is driven by both quantum and classical fluctuations, unlike the single-mode case, which only is liable to classical noise. (Quantum fluctuations diminish as the atom number N increases in a single mode cavity [12].) Indeed, while interactions in the single-mode case are infinite-ranged, the fluctuations in the quasimomentum space are limited to 0D points given by $\pm n = k_0 R$. The space liable to these fluctuations in the multimode case is much larger, occupying the 1D lines delimited above. As the number of degenerate modes increases, the lines the soft modes trace form a quasi-continuous distribution in quasimomentum space: breaking this quasi-continuous symmetry induces Goldstone modes in the ordered phase that manifest as phonon-like excitations of the atomic positions. The order exhibited by this quantum Brazovskii transition is quite unusual—a superfluid smectic quantum liquid crystal—and worthy of exploration both in its own right and due to the relevance of these to technologically relevant strongly correlated materials [7, 8, 64, 65]. Geometrical frustration destroys this quantum liquid crystal if a stack of 2D BECs are trapped in a lamellar pattern spanning either side of the cavity axis. The ensuing phase should resemble a superfluid glass [7, 8, 66].

Each of these manifestations of quantum soft matter may be heralded by telltale time or spatial correlations in the emission from the cavity mode as threshold is reached [7, 8]. Bragg peaks in the atomic momentum distribution emerge in the single-mode case [48, 53] and are a direct indication that a fraction of the matter wave has self-organized into a periodic pattern. In the supersmectic phase, these Bragg peaks should broaden into arcs, just as in the case of x-ray scattering off classical liquid crystals [67].

Fixing the positions of spinful atoms at random locations within the cavity modes using an external, static optical lattice sets the stage for exploring spin-glass physics and the closely associated architectures for neuromorphic photonic computation [11–16]. Atoms with one spin state coupled to a transverse pump field, but with the other state coupled to the cavity mode(s), exchange spin-flip excitations when the Raman-resonance condition is off by a detuning $\Delta_C \gg \kappa$. In a single-mode cavity, this disordered XY-spin model realizes a 'Mattis model' resulting in a spin-helix texture [68]. Adding additional modes to the cavity frustrates the interactions. With a sufficient number of degenerate modes, the system should no longer support long-range spatial spin order, though order may develop in time, resulting in the aging and arrested dynamics characteristic of a spin glass. Observations of system dynamics over many decades in time are possible from the short-time, quantum-fluctuation driven regime to the long-time, thermal-fluctuation driven regime.

6. Conclusion

Future work will strive to demonstrate the use of this novel adjustable-length cavity and BEC multimode cavity QED apparatus in searches for these exotic states of quantum matter. The strong and spatially dynamic light–matter interaction provided by cavity QED may also be exploited for applications outside the exploration of many-body physics such as quantum information processing [69], cavity optomechanics [70] and sensing [71].

Acknowledgments

References

[1] Ritsch H, Domokos P, Brennecke F and Esslinger T 2013 *Mod. Phys. Rev.* **85** 553
[2] Bloch I, Dalibard J and Zwerger W 2008 *Mod. Phys. Rev.* **80** 885
[3] Cirac J I and Zoller P 2012 *Nat. Phys.* **8** 264
[4] Yan B, Moses S A, Gadway B, Covey J P, Hazzard K R A, Rey A M, Jin D S and Ye J 2013 *Nature* **501** 521–5
[5] Asbóth J, Domokos P, Ritsch H and Vukics A 2005 *Phys. Rev.* A **72** 053417
[6] Szymańska M H, Keeling J and Littlewood P B 2006 *Phys. Rev. Lett.* **96** 230602
[7] Gopalakrishnan S, Lev B L and Goldbart P M 2009 *Nat. Phys.* **5** 845
[8] Gopalakrishnan S, Lev B L and Goldbart P M 2010 *Phys. Rev.* A **82** 043612
[9] Torre E G D, Diehl S, Lukin M D, Sachdev S and Strack P 2013 *Phys. Rev.* A **87** 023831

[10] Münstermann P, Fischer T, Maunz P, Pinkse P W H and Rempe G 2000 *Phys. Rev. Lett.* **84** 4068

[11] Gopalakrishnan S, Lev B L and Goldbart P M 2011 *Phys. Rev. Lett.* **107** 277201

[12] Strack P and Sachdev S 2011 *Phys. Rev. Lett.* **107** 277202

[13] Müller M, Strack P and Sachdev S 2012 *Phys. Rev. A* **86** 023604

[14] Buchhold M, Strack P, Sachdev S and Diehl S 2013 *Phys. Rev. A* **87** 063622

[15] Gopalakrishnan S, Lev B L and Goldbart P M 2011 *Phil. Mag.* **92** 353

[16] Marandi A, Wang Z, Takata K, Byer R L and Yamamoto Y 2014 *Nat. Photonics*

[17] Grimm R, Weidemüller M and Ovchinnikov Y 2000 *Adv. At. Mol. Opt. Phys.* **42** 95

[18] Tanji-Suzuki H, Leroux I D, Schleier-Smith M H, Cetina M, Grier A T, Simon J and Vuletić V 2011 *Adv. At. Mol. Opt. Phys.* **60** 201

[19] Siegman A E 1986 *Lasers* (Mill Valley, CA: University Science Books)

[20] Vuletić V, Chan H and Black A 2001 *Phys. Rev. A* **64** 033405

[21] Chan H 2003 Cavity cooling of cesium atoms *PhD Thesis* Stanford University

[22] Drever R W P, Hall J L, Kowalski F V, Hough J, Ford G M, Munley A J and Ward H 1983 *Appl. Phys.* B **31** 97

[23] Black E D 2001 *Am. J. Phys.* **69** 79

[24] Keller M 2004 Quantenoptik mit gespeicherten 40Ca+-ionen *PhD Thesis* Technische Universität Munchen

[25] Koch M 2011 Classical and quantum dynamics of a strongly coupled atom-cavity system *PhD Thesis* Technische Universität Munchen

[26] Horak P, Ritsch H, Fischer T, Maunz P, Puppe T, Pinkse P W H and Rempe G 2002 *Phys. Rev. Lett.* **88** 043601

[27] Chan H, Black A and Vuletić V 2003 *Phys. Rev. Lett.* **90** 063003

[28] Black A, Chan H and Vuletić V 2003 *Phys. Rev. Lett.* **91** 203001

[29] Wickenbrock A, Hemmerling M, Robb G R M, Emary C and Renzoni F 2013 *Phys. Rev. A* **87** 043817

[30] Hood C J, Kimble H J and Ye J 2001 *Phys. Rev. A* **64** 033804

[31] Lin Y J, Perry A R, Compton R L, Spielman I B and Porto J V 2009 *Phys. Rev. A* **79** 063631

[32] Metcalf H J and van der Straten P 1999 *Laser Cooling and Trapping* (New York: Springer)

[33] Gustavson T L, Chikkatur A P, Leanhardt A E, Görlitz A, Gupta S, Pritchard D E and Ketterle W 2001 *Phys. Rev. Lett.* **88** 020401

[34] Kimble H J 1998 *Phys. Scr.* **T76** 127

[35] Hood C, Lynn T, Doherty A, Parkins A and Kimble H 2000 *Science* **287** 1447

[36] Cohen-Tannoudji C, Dupont-Roc J and Grynberg G 1998 *Atom–Photon Interactions* (New York: Wiley)

[37] Arnold K J, Baden M P and Barrett M D 2012 *Phys. Rev. Lett.* **109** 153002

[38] Domokos P, Salzburger T and Ritsch H 2002 *Phys. Rev. A* **66** 043406

[39] Lev B L, Vukics A, Hudson E R, Sawyer B C, Domokos P, Ritsch H and Ye J 2008 *Phys. Rev. A* **77** 023402

[40] Domokos P and Ritsch H 2002 *Phys. Rev. Lett.* **89** 163002

[41] Dimer F, Estienne B, Parkins A S and Carmichael H J 2007 *Phys. Rev. A* **75** 013804

[42] Larson J, Damski B, Morigi G and Lewenstein M 2008 *Phys. Rev. Lett.* **100** 050401

[43] Nagy D, Szirmai G and Domokos P 2008 *Eur. Phys. J. D* **48** 127

[44] Nagy D, Kónya G, Szirmai G and Domokos P 2010 *Phys. Rev. Lett.* **104** 130401

[45] Fernandez-Vidal S, de Chiara G, Larson J and Morigi G 2010 *Phys. Rev. A* **81** 043407

[46] Keeling J, Bhaseen M J and Simons B D 2010 *Phys. Rev. Lett.* **105** 043001

[47] Baumann K, Guerlin C, Brennecke F and Esslinger T 2010 *Nature* **464** 1301

[48] Baumann K, Mottl R, Brennecke F and Esslinger T 2011 *Phys. Rev. Lett.* **107** 140402

[49] Mottl R, Brennecke F, Baumann K, Landig R, Donner T and Esslinger T 2012 *Science* **336** 1570

[50] Arnold K J, Baden M P and Barrett M D 2012 *Phys. Rev. Lett.* **109** 153002

[51] Brennecke F, Mottl R, Baumann K, Landig R, Donner T and Esslinger T 2013 *Proc. Natl Acad. Sci. USA* **110** 11763

[52] Baden M P, Arnold K J, Grimsmo A L, Parkins S and Barrett M D 2014 *Phys. Rev. Lett.* **113** 020408

[53] Keßler H, Klinder J, Wolke M and Hemmerich A 2014 *Phys. Rev. Lett.* **113** 070404

[54] Colombe Y, Steinmetz T, Dubois G, Linke F, Hunger D and Reichel J 2007 *Nature* **450** 272

[55] Brennecke F, Donner T, Ritter S, Bourdel T, Köhl M and Esslinger T 2007 *Nature* **450** 268

[56] Slama S, Bux S, Krenz G, Zimmermann C and Courteille P W 2007 *Phys. Rev. Lett.* **98** 053603

[57] Schmidt D, Tomczyk H, Slama S and Zimmermann C 2014 *Phys. Rev. Lett.* **112** 115302

[58] Greenberg J A and Gauthier D J 2012 *Europhys. Lett.* **98** 24001

[59] Greenberg J A and Gauthier D J 2012 *Phys. Rev. A* **86** 013823

[60] Tesio E, Robb G R M, Ackemann T, Firth W J and Oppo G L 2012 *Phys. Rev. A* **86** 031801

[61] Labeyrie G, Tesio E, Gomes P M, Oppo G L, Firth W J, Robb G R M, Arnold A S, Kaiser R and Ackemann T 2014 *Nat. Photonics* **8** 321

[62] Brazovskii S 1975 *Sov. Phys.—JETP* **41** 85

[63] Hohenberg P and Swift J 1995 *Phys. Rev. E* **52** 1828

[64] Jonathan Keeling J B and Simons B 2010 *Physics* **3** 88

[65] Fradkin E and Kivelson S A 2012 *Nat. Phys.* **8** 864

[66] Boninsegni M, Prokof'ev N and Svistunov B 2006 *Phys. Rev. Lett.* **96** 105301

[67] Chaikin P and Lubensky T 1995 *Principles of Condensed Matter Physics* (Cambridge: Cambridge University Press)

[68] Weissman M and Wolynes P 1992 *Phys. Rev. B* **46** 14209

[69] Kimble H J 2008 *Nature* **453** 1023

[70] Stamper-Kurn D M 2014 Cavity optomechanics with cold atosm *Cavity Optomechanics* ed M Aspelmeyer *et al* (Berlin: Springer) chapter 13

[71] Schreppler S, Spethmann N, Brahms N, Botter T, Barrios M and Stamper-Kurn D M 2014 *Science* **344** 1486